Figures and figure supplements

GluA3 subunits are required for appropriate assembly of AMPAR GluA2 and GluA4 subunits on cochlear afferent synapses and for presynaptic ribbon modiolar–pillar morphology

Mark A Rutherford *et al*.

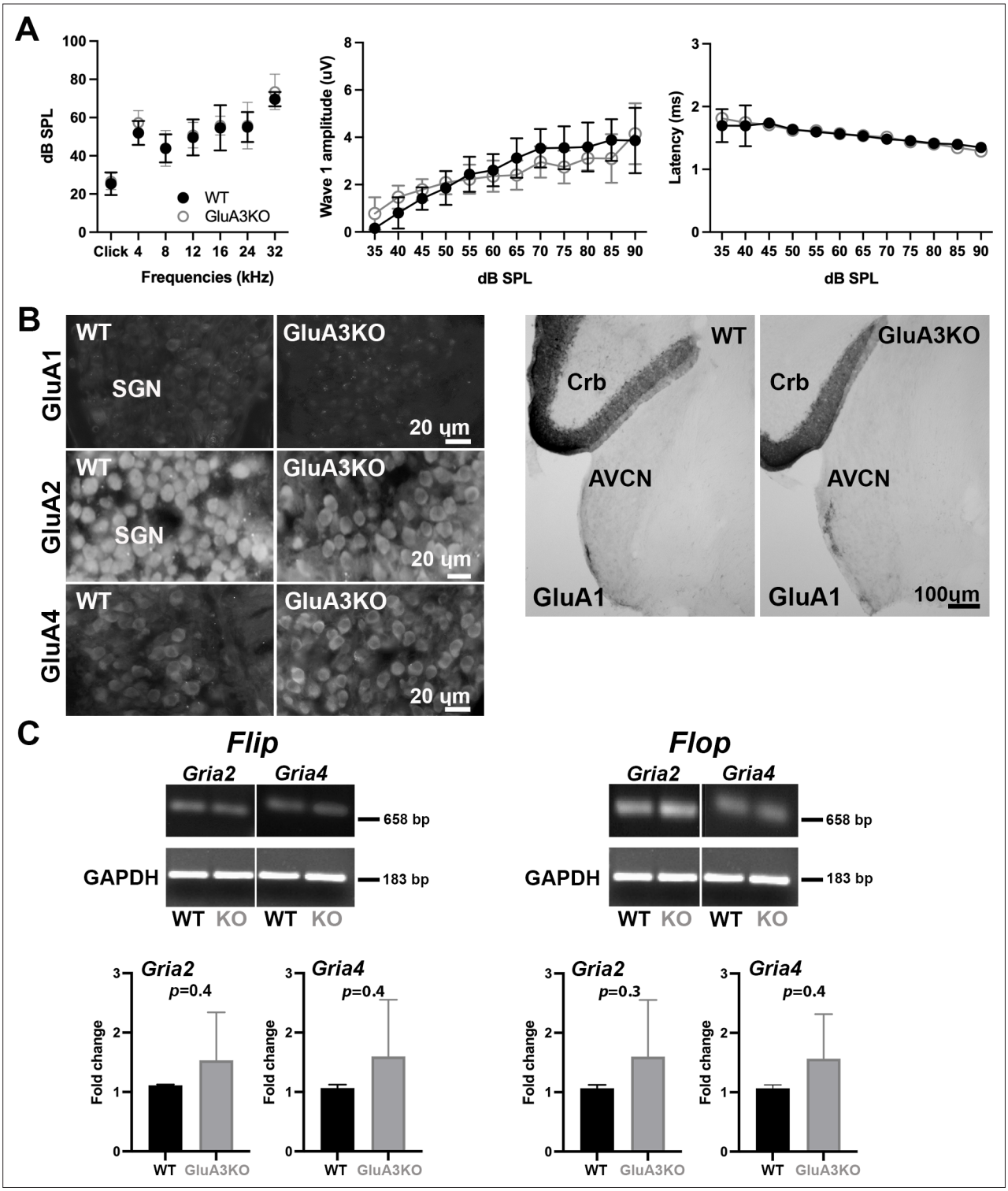

Figure 1. ABRs, GluA1 and GluA2 immunolabeling and qRT-PCR in GluA3^{WT} and GluA3^{KO}. (**A**) Mean ABR thresholds (± standard deviation [SD]) were similar between male GluA3^{WT} and GluA3^{KO} mice ($F_{(1, 168)}$ = 2.659, p = 0.11; two-way analysis of variance (ANOVA); GluA3^{WT} *n* = 13; GluA3^{KO} *n* = 13). In GluA3^{WT} and GluA3^{KO}, there was a main effect of sound frequency ($F_{(6, 168)}$ = 78.78, p < 0.0001). For ABR wave-1 amplitudes (± SD), there was an effect of sound ilevel ($F_{(11, 192)}$ = 49.62, p < 0.0001), but mean amplitudes were similar between genotypes ($F_{(1, 292)}$ = 2.458, p = 0.118; two-way ANOVA). For ABR wave-1 latencies (± SD), there was a main effect of sound level in both genotypes ($F_{(1, 288)}$ = 47.11, p < 0.0001) and mean latencies were similar between GluA3^{WT} and GluA3^{KO} mice ($F_{(1, 288)}$ = 0.1273, p = 0.7215; two-way ANOVA). (**B**) Micrographs show immunolabeling for GluA1, GluA2, and GluA4 on spiral ganglion neuron (SGN) somata, and for GluA1 on the anteroventral cochlear nucleus (AVCN) and cerebellum (Crb) of GluA3^{WT} and GluA3^{KO} mice.

Figure 1 continued on next page

Figure 1 continued

Immunolabeling for GluA2 and GluA4 is observed on SGNs of both genotypes. In contrast, immunolabeling for GluA1 was not observed on SGNs nor in the AVCN of $GluA3^{WT}$ or $GluA3^{KO}$ mice, but was observed in the cerebellar Bergmann glia of both genotypes. Scale bars: 20 and 100 µm. (**C**) Images of *Gria2* and *Gria4 flip* and *flop*, and GAPDH gels of $GluA3^{WT}$ and $GluA3^{KO}$ inner ears. Histograms show fold change (± SD) of qRT-PCR product. Paired *t*-test, two-tailed; bp: base pairs.

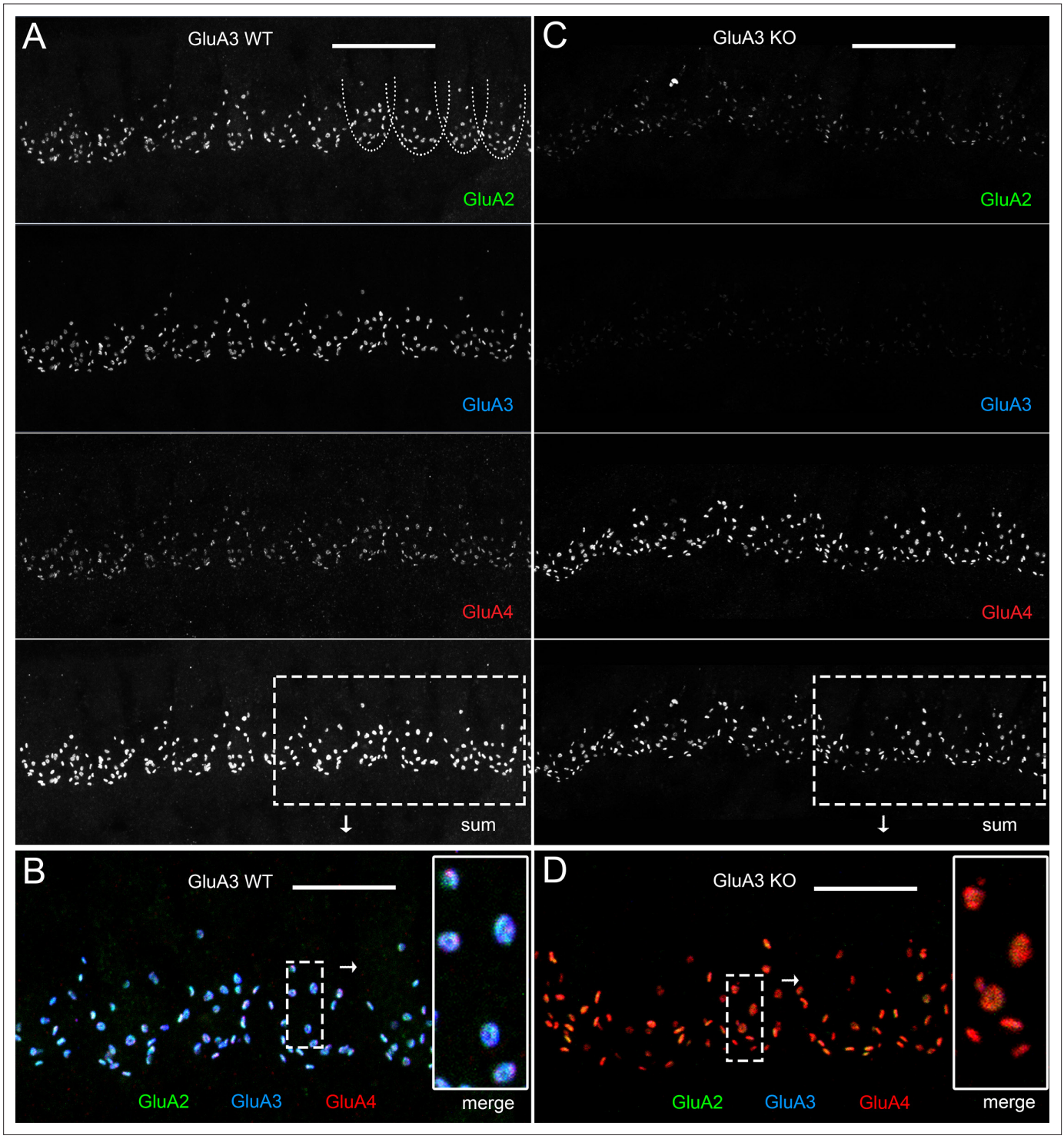

Figure 2. Immunohistofluorescence of α-amino-3-hydroxy-5-methyl-4-isoxazole propionic acid receptor (AMPAR) pore-forming subunits GluA2, 3, and 4 on spiral ganglion neuron postsynaptic terminals in the organ of Corti. Confocal microscope immunofluorescence images of afferent ribbon synapses in organ of Corti whole-mount samples from GluA3^{WT} (left) and GluA3^{KO} mice (right) in the mid-cochlea. Anti-GluA2 (green), -GluA3 (blue), and -GluA4 (red) labels the postsynaptic AMPAR subunits encoded by the *Gria2*, *Gria3*, and *Gria4* genes, respectively. Each subpanel displays synaptic puncta of approximately 12 inner hair cells (IHCs). Scale bars: 20 µm (**A, C**); 10 µm (**B, D**). (**A**) From top to bottom: GluA3^{WT} in grayscale for anti-GluA2, 3, 4, and the sum of the three. In the GluA2 subpanel, the basolateral membranes of four IHCs are indicated by dashed curves. (**B**) Merged color image of the region of interest indicated by the dashed rectangle in panel A. Inset on right: enlargement of the dashed rectangular region of interest on left shows five postsynaptic AMPA receptor arrays of ribbon synapses from one IHC. (**C**) From top to bottom: GluA3^{KO} in grayscale for anti-GluA2, 3, 4, and the sum of the three. (**D**) Merged color image of the region of interest indicated in panel C. Inset: enlargement of a rectangular region of interest shows several postsynaptic AMPAR arrays of ribbon synapses from one IHC.

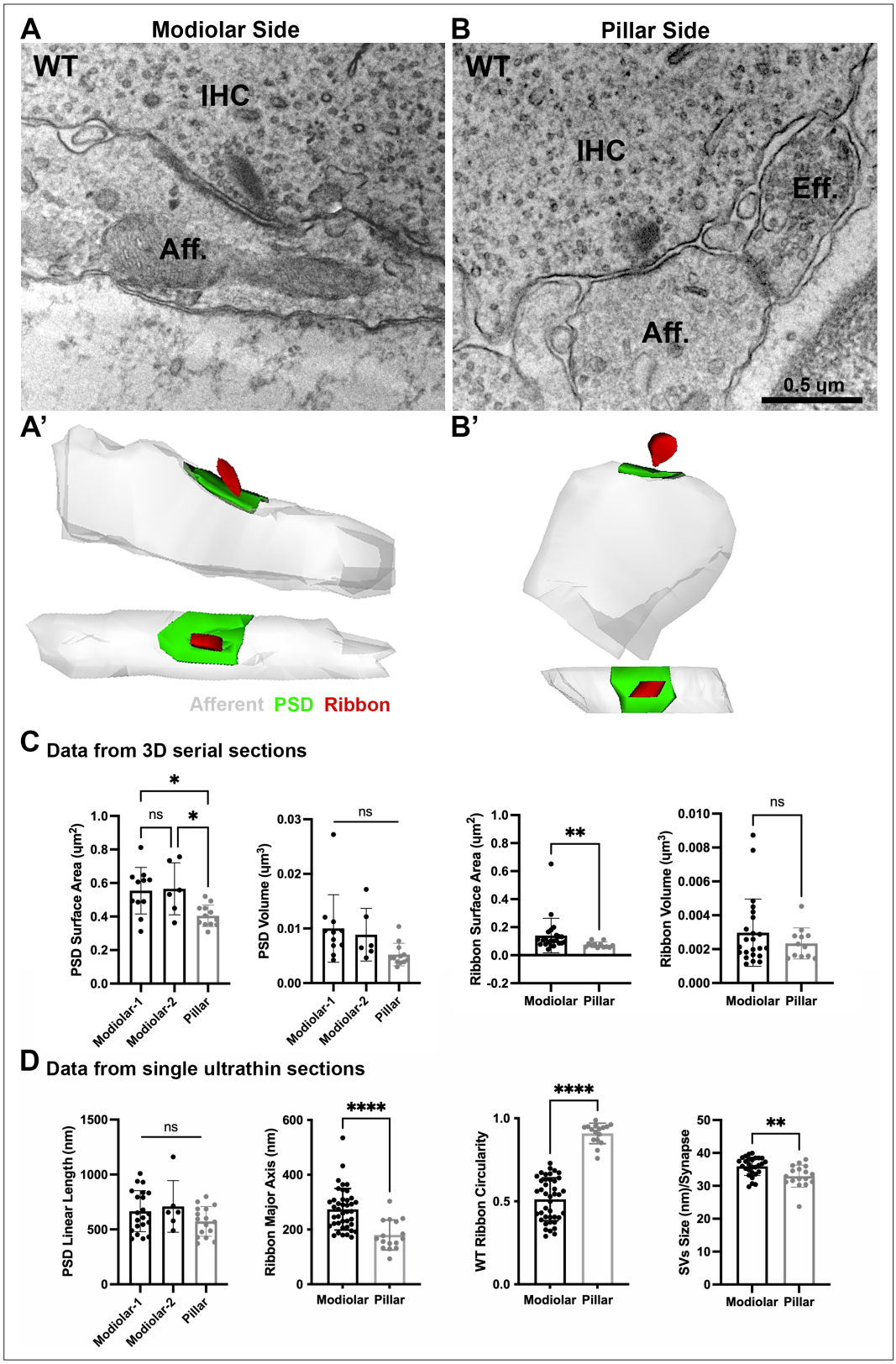

Figure 3. Ultrastructural features of GluA3^{WT} IHC-ribbon mid-cochlear synapses. Transmission electron microscopy (TEM) micrographs of IHC synapses on the modiolar (**A**) and pillar sides (**B**). Aff.: afferent; IHC: inner hair cell; Eff.: efferent terminal. Scale bar: 0.5 µm. (**A', B'**) Three-dimensional (3D) reconstructions of the IHC-ribbon synapses are shown in A and B. Representative serial electron micrograph images of modiolar- and pillar-side ribbon synapses

Figure 3 continued on next page

Figure 3 continued

are shown in ***Figure 3—figure supplement 1***. (**C**) Plots of the quantitative data of the surface area, and volume of the postsynaptic densities (PSDs) and ribbons obtained from the 3D reconstructions of GluA3^{WT} mice. The error bar corresponds to ± standard deviation (SD). (**D**) Plots of the quantitative data from single ultrathin sections of the linear length of the PSD, major axis, and circularity of the ribbons, and the average size of synaptic vesicles (SVs)/synapse of GluA3^{WT} mice. The error bar corresponds to ± SD; one-way Anova * $p < 0.05$, ns: not significant; Mann-Whitney two-tailed U-test, ** $p < 0.01$, *** $p < 0.0001$, ns: not significant.

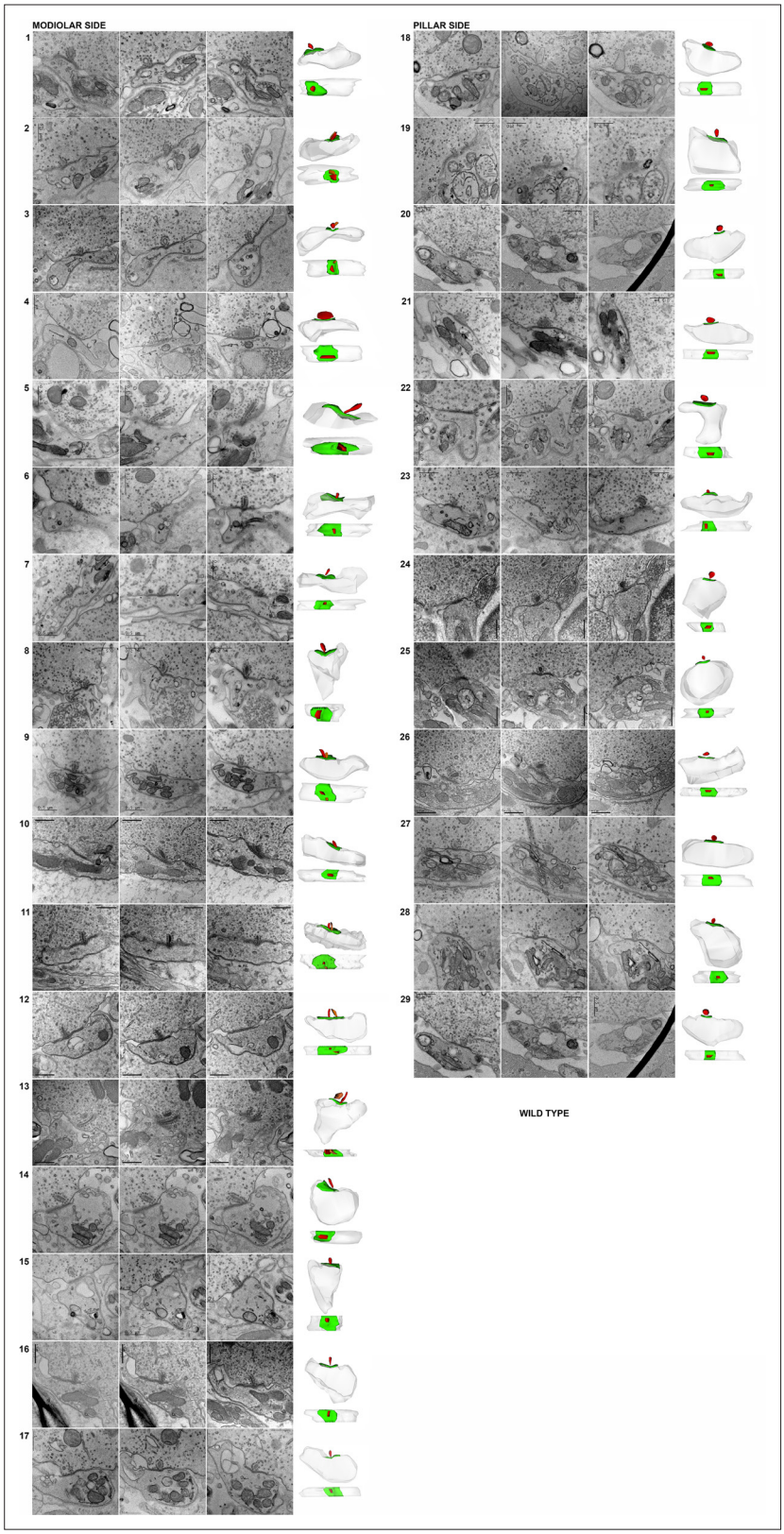

Figure 3—figure supplement 1. Representative serial electron micrographs and corresponding three-dimensional (3D) reconstructions of modiolar- or pillar-side inner hair cell (IHC)-ribbon synapses of the GluA3^{WT} mice. Synapses #10 and #24 correspond to the synapses shown in ***Figure 3***. Scale bar: 0.5 µm.

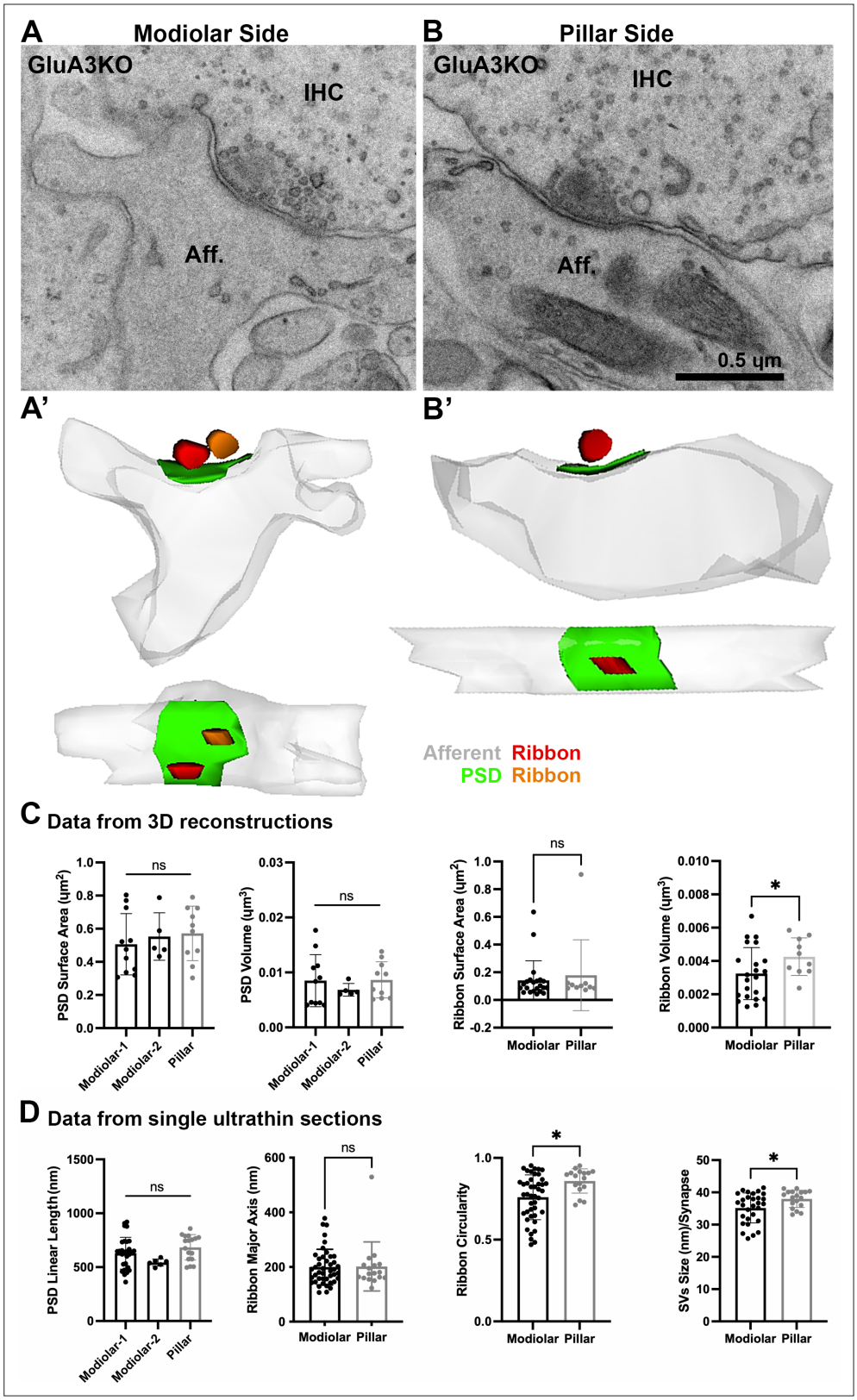

Figure 4. Ultrastructural features of GluA3^{KO} IHC-ribbon mid-cochlear synapses. Transmission electron microscopy (TEM) micrographs of IHC synapses on the modiolar (**A**) and pillar sides (**B**) of GluA3^{KO} mice. Aff.: afferent; IHC: inner hair cell. Scale bar: 0.5 µm. (**A', B'**) Three-dimensional reconstructions of the IHC-ribbon synapses are shown in A and B. Representative serial electron micrograph images of modiolar- and pillar-side ribbon synapses are

Figure 4 continued on next page

Figure 4 continued

shown in ***Figure 4—figure supplement 1***. (**C**) Plots of the quantitative data of the surface area and volume of the postsynaptic densities (PSDs) and ribbons obtained from the 3D reconstructions of GluA3^{KO} mice. The error bar corresponds to ± standard deviation (SD). (**D**) Plots of the quantitative data from single ultrathin sections of the linear length of the PSD, major axis and circularity of the ribbons and the average size of synaptic vesicles (SVs)/synapse of GluA3^{KO} mice. The error bar corresponds to ± SD; one-way ANOVA, ns: not significant; Mann-Whitney two-tailes U-test, * $p < 0.05$, ns: not significant.

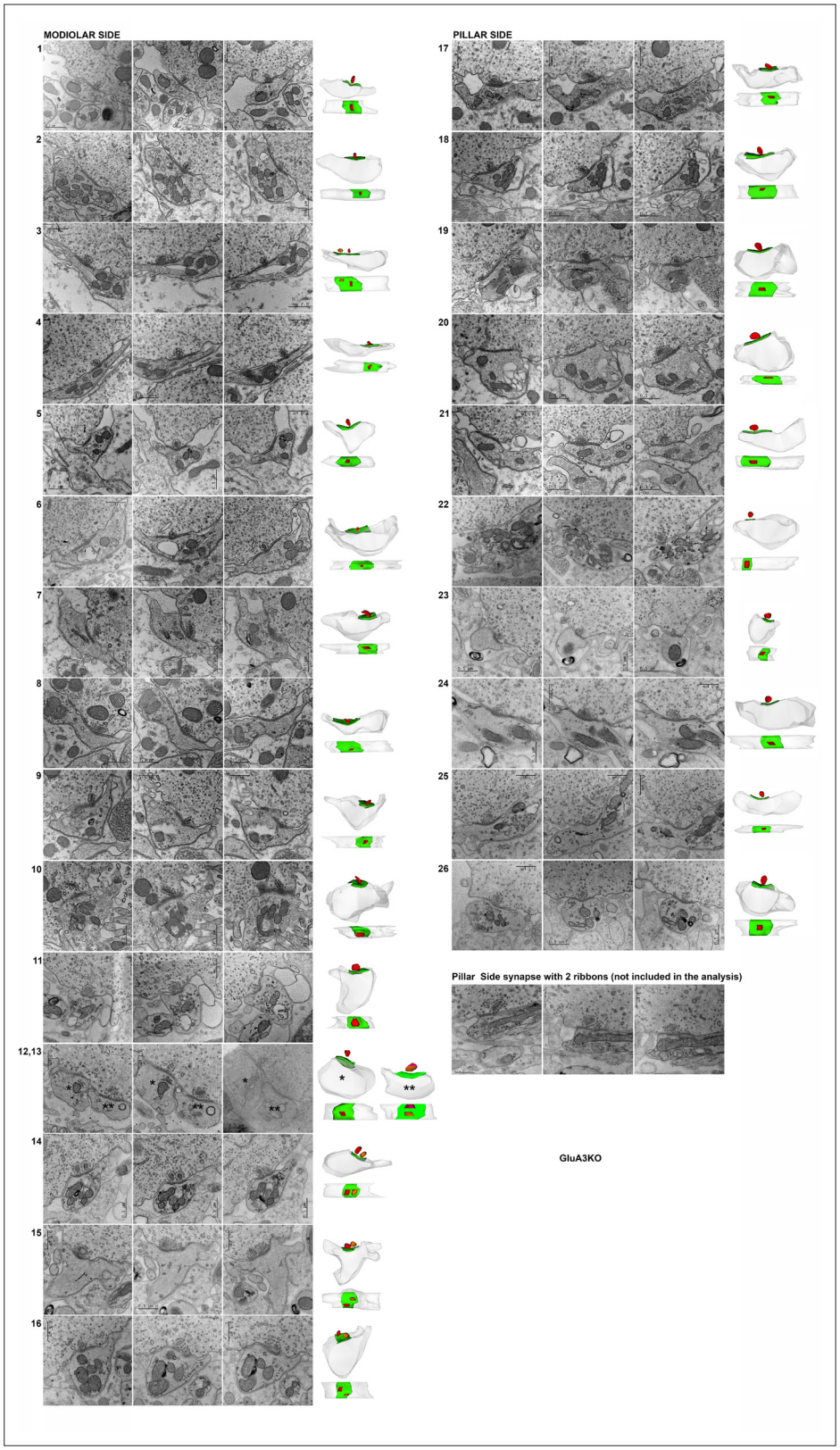

Figure 4—figure supplement 1. Representative serial electron micrographs and corresponding three-dimensional (3D) reconstructions of modiolar- or pillar-side inner hair cell (IHC)-ribbon synapses of the GluA3^{KO} mice. Synapses #15 and #24 correspond to the synapses shown in ***Figure 4***. Representative serial electron micrographs of one pillar-side synapse with two ribbons; this synapse was not included in our analysis. Scale bar: 0.5 µm.

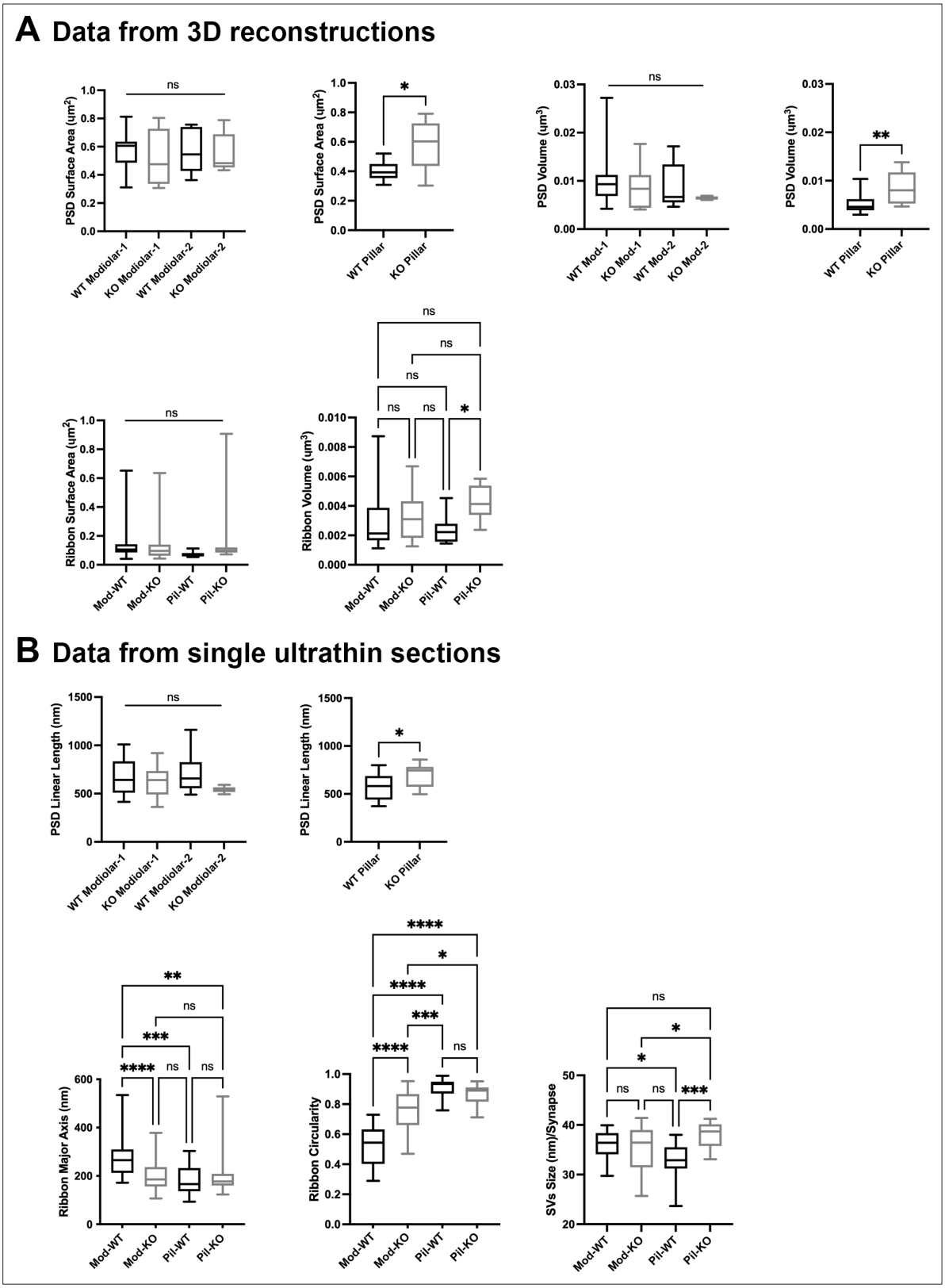

Figure 5. Inner hair cell (IHC) modiolar–pillar structural differences in presynaptic ribbon size, ribbon shape, and vesicle size seen in GluA3^{WT} were diminished or reversed in GluA 3^{KO}. (**A**) Whisker plots show the quantitative data of the surface area and volume of the postsynaptic density (PSD) and ribbon volume of GluA3^{WT} (black) and GluA3^{KO} (gray) mice. The error bar corresponds to ± standard deviation (SD). (**B**) Whisker plots of the linear length of the PSD, major axis, and circularity of the ribbons of GluA3^{WT} (black) and GluA3^{KO} (gray) mice. Column histogram of the size of synaptic vesicles (SVs)

Figure 5 continued on next page

Figure 5 continued

of GluA3^{WT} (black) and GluA3^{KO} (gray). The error bar corresponds to ± SD; one-way ANOVA, * $p < 0.05$, ** $p < 0.01$, *** $p < 0.005$, $p < 0.0001$, ns: not significant; Mann-Whitney two-tailed U-test, * $p < 0.05$, ** $p < 0.001$.

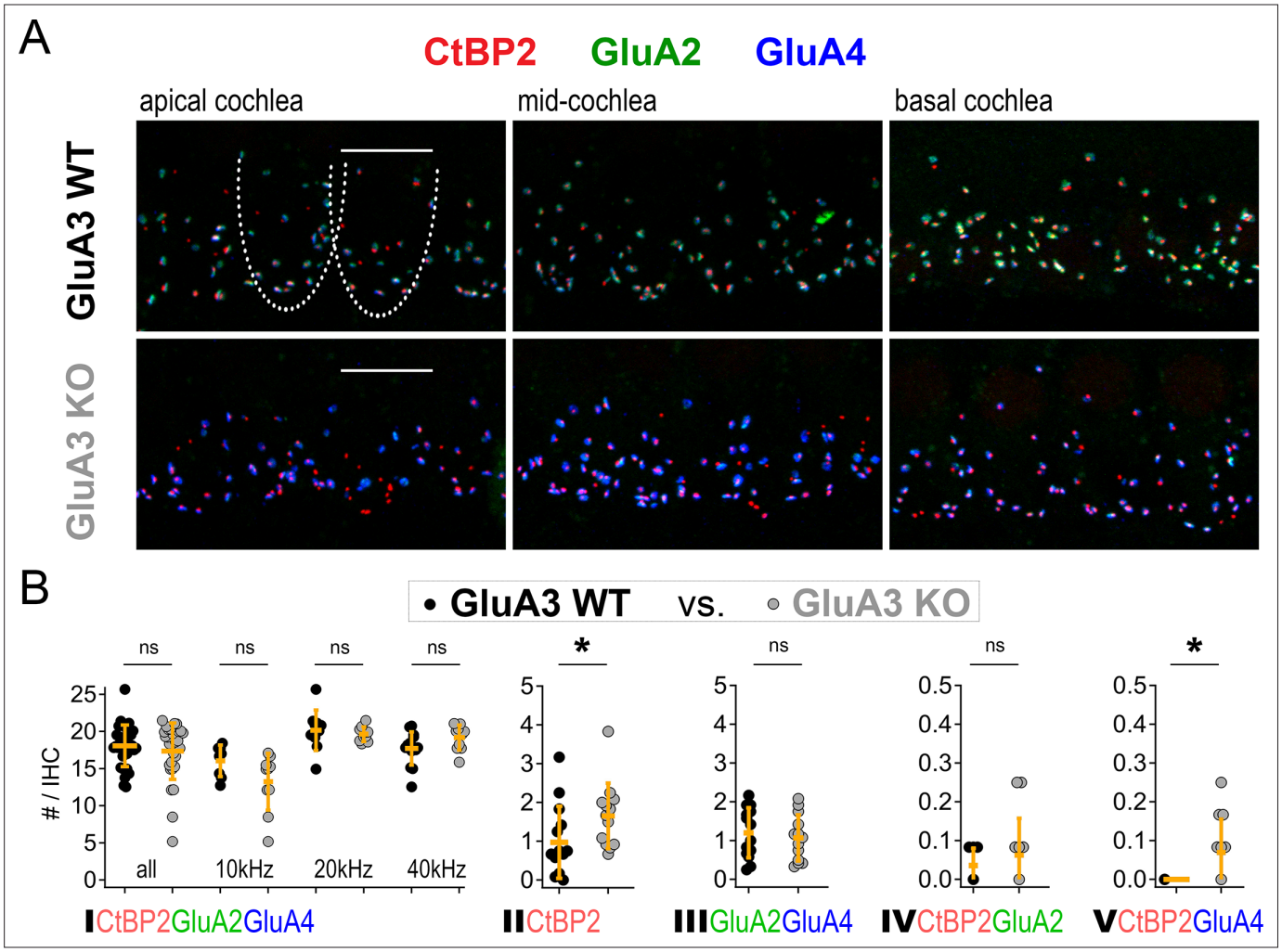

Figure 6. Inner hair cell (IHC)-ribbon synapse counts in 5-week-old male GluA3^{WT} and GluA3^{KO} mice. (**A**) Confocal microscope immunofluorescence images of afferent ribbon synapses in organ of Corti whole-mount samples from GluA3^{WT} (upper) and GluA3^{KO} mice (lower) in the apical, middle, and basal cochlea (left, middle, and right). Anti-CtBP2 labels the Ribeye protein in presynaptic ribbons (red); Anti-GluA2 labels the postsynaptic α-amino-3-hydroxy-5-methyl-4-isoxazole propionic acid receptor (AMPAR) subunit encoded by the *Gria2* gene (green); Anti-GluA4 labels the AMPAR subunit encoded by *Gria4* (blue). Each subpanel displays synaptic puncta of approximately four IHCs. Scale bar: 10 µm. (**B**) Quantification of ribbon synapse numbers in images from GluA3^{WT} (black: 2990 synapses; n = 32 images; 5 mice) and GluA3^{KO} (gray: n = 2814 synapses; n = 30 images; 5 mice). Each point represents the mean number of synapses per IHC per image; approximately 12 IHCs per image and 6 images per cochlea. (I) Paired synapses per IHC were similar in number for the whole cochlea (p = 0.94, U: 484, n_{WT} = 32, n_{KO} = 30) and in each of three tonotopic regions centered at 10 kHz (p = 0.08, U: 59, n_{WT} = 8, n_{KO} = 10), 20 kHz (p = 0.41, U: 61, n_{WT} = 10, n_{KO} = 10), or 40 kHz (p = 0.10, U: 42, n_{WT} = 14, n_{KO} = 10). (II) Lone or 'orphaned' ribbons (CtBP2-only) were significantly more frequent in GluA3^{KO} (p = 0.021, U: 44, n_{WT} = 14, n_{KO} = 13). (III) Ribbonless synapses (GluA2 + GluA4) were similar in number (p = 0.67, U: 100, n_{WT} = 14, n_{KO} = 13). (IV) Paired synapses lacking GluA4 (CtBP2 + GluA2) were similar in number (p = 0.81, U: 39, n_{WT} = 7, n_{KO} = 12). (V) Paired synapses lacking GluA2 (CtBP2 + GluA4) were observed in GluA3^{KO} (p = 0.028, U: 21, n_{WT} = 7, n_{KO} = 12) but not in GluA3^{WT}. Mann-Whitney two-tailed U-test; * p < 0.05, ns: not significant.

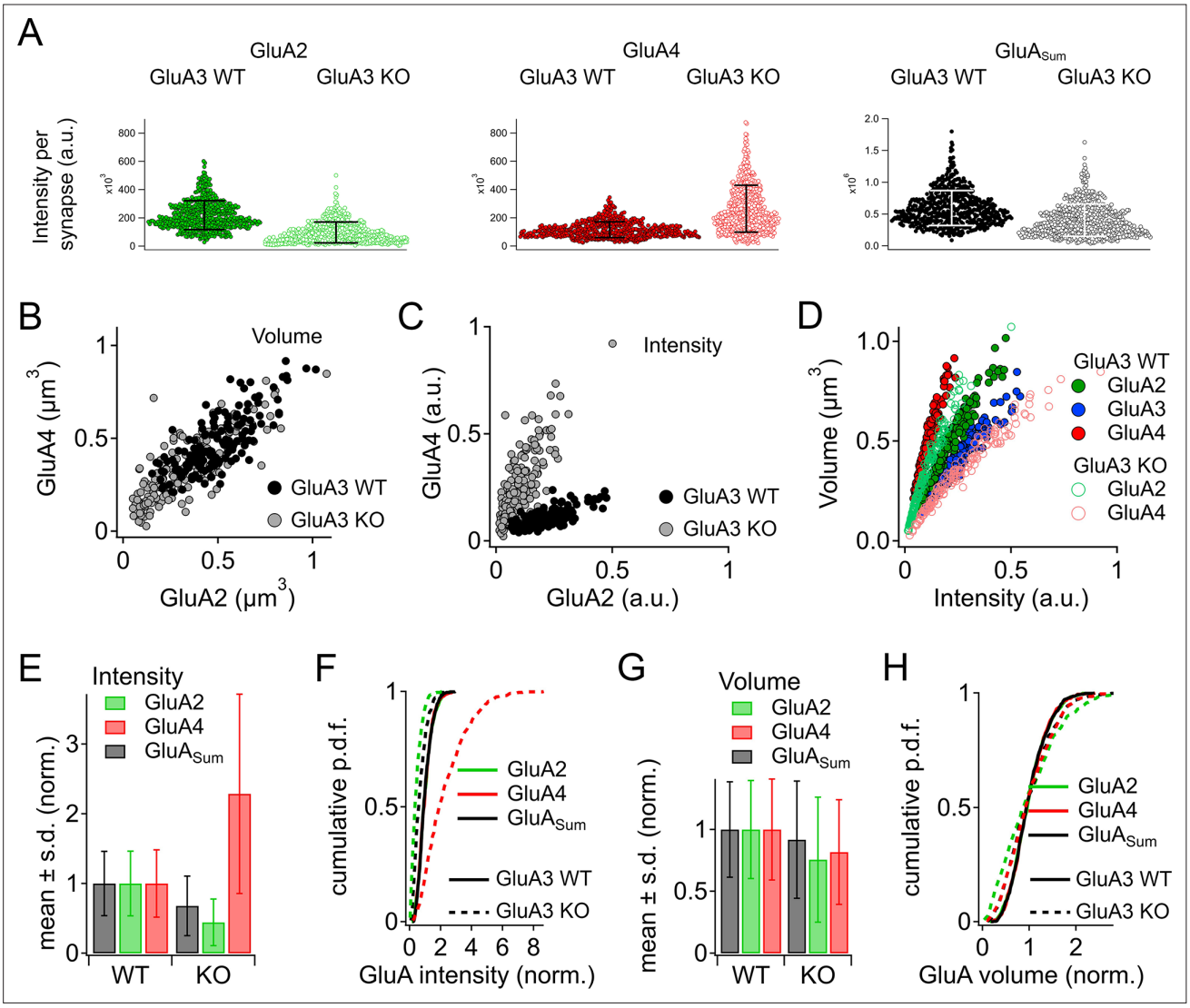

Figure 7. Alteration of α-amino-3-hydroxy-5-methyl-4-isoxazole propionic acid receptor (AMPAR) subunit expression in GluA3^{KO} mice. (**A**) From images like in ***Figure 2***: Summed pixel intensity per synapse (raw values, a.u.) for GluA2 (green), GluA4 (blue), and GluA$_{Sum}$ (black). In each subpanel, GluA3^{WT} is on left and GluA3^{KO} is on right. Bars show mean ± standard deviation (SD); *n* = 3 mid-cochlear images per genotype, assessed further in panels **E–H**. (**B**) Volume analysis of two exemplar images showing GluA4 vs. GluA2 volume per synapse (µm^3) in the mid-cochlea of GluA3^{WT} (black, *n* = 148 synapses) and GluA3^{KO} (gray, *n* = 166 synapses). The distribution of GluA4 and GluA2 puncta are shifted to smaller volumes in GluA3^{KO}, although the upper ranges are unchanged. (**C**) Intensity analysis of the synapses in panel **B** (summed pixel intensity per synapse) reveals an increase in GluA4 and decrease in GluA2 immunofluorescence in GluA3^{KO}. Intensity values were normalized to the maximum synapse intensity for GluA4. (**D**) Volume (µm^3) vs. summed pixel intensity (norm.) per synapse for GluA3^{WT} (filled circles) and GluA3^{KO} (open circles) for GluA2, 3, and 4 puncta (green, blue, and red). The positive correlation is slightly sublinear. (**E**) Intensity analysis (sum of pixel intensities per synapse) of postsynaptic puncta grouped from GluA3^{WT} (*n* = 545 synapses from 3 images) or GluA3^{KO} cochlea (*n* = 513 synapses from 3 images) shows reduction of overall GluA intensity (GluA$_{Sum}$ = GluA2 + GluA3 + GluA4, gray) and reduction in GluA2 intensity (green) with increase in GluA4 intensity (red) in GluA3^{KO}. Data are normalized to the mean WT synapse intensity per group for GluA2, GluA4, or GluA$_{Sum}$. (**F**) Normalized data as in panel E displayed as cumulative distributions for GluA3^{WT} (solid line) and GluA3^{KO} (dashed lines). The overall intensity in GluA3^{KO} (black dashed line, GluA$_{Sum}$) is reduced relative to GluA3^{WT} (solid black line) due to lack of GluA3 and reduction in GluA2 (green) despite the relatively large increase in GluA4 (red). (**G**) GluA puncta volume analysis reveals a reduction of GluA2 and GluA4 volume per synapse in GluA3^{KO} relative to GluA3^{WT}. Data are normalized to the mean WT synapse volume per group for GluA2, GluA4, or GluA$_{Sum}$. (**H**) Data in panel G displayed as cumulative distributions. Instead of normalizing to the WT group mean as in panels E–G, here data were normalized to each image mean to visualize differences in the shape of the distributions between GluA3^{WT} and GluA3^{KO}.

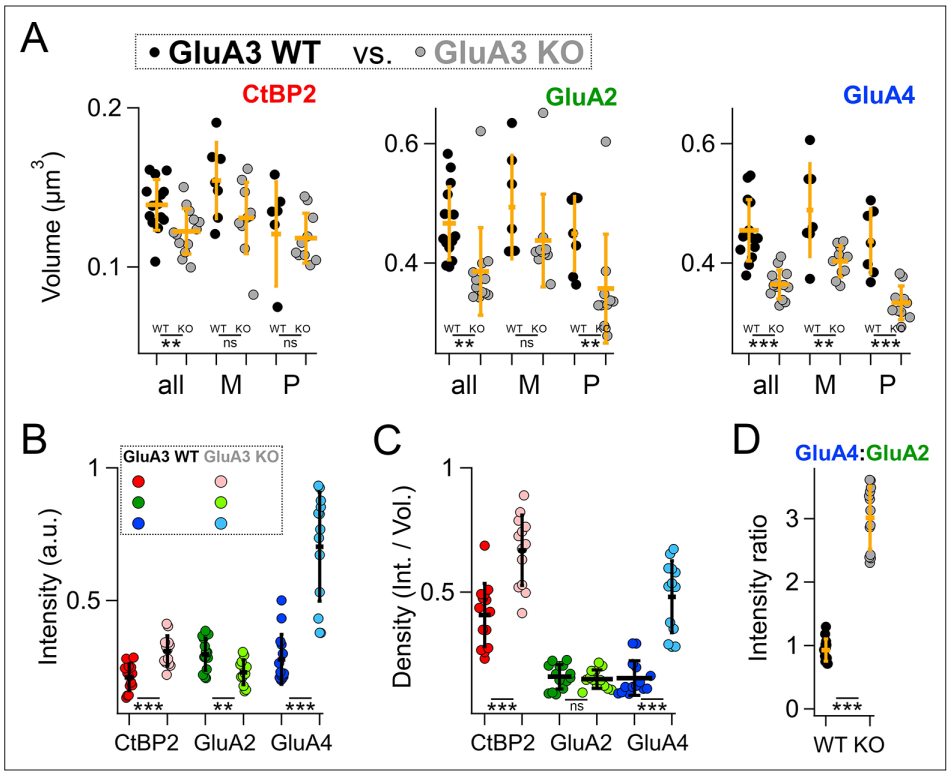

Figure 8. Modiolar- and pillar-side volume, intensity, and density of presynaptic ribbon and postsynaptic α-amino-3-hydroxy-5-methyl-4-isoxazole propionic acid receptor (AMPAR) subunits. (**A**) Quantification of CtBP2, GluA2, or GluA4 mean volume per image for GluA3^{WT} (black, n = 2990 synapses from 14 images) compared to GluA3^{KO} (gray, n = 2814 synapses from 14 images). Each point represents an image mean. Gold bars are mean ± standard deviation (SD). For CtBP2, there is an overall reduction in volume in GluA3^{KO} (p = 0.008, U: 144, n_{WT} = 14, n_{KO} = 13). For GluA2, the overall volume reduction in GluA3^{KO} (p = 0.0001, U: 168, n_{WT} = 14, n_{KO} = 13) resulted from smaller puncta on the pillar side of GluA3^{KO} relative to GluA3^{WT} (p = 0.0083; U: 90, n_{WT} = 7, n_{KO} = 10) but not on the modiolar side (p = 0.063). For GluA4, the overall volume reduction in GluA3^{KO} (p = 4.9e^{-6}; U: 176, n_{WT} = 14, n_{KO} = 13) resulted from smaller puncta on the pillar side of GluA3^{KO} (p = 0.0004; U: 96, n_{WT} = 7, n_{KO} = 10) and on the modiolar side of GluA3^{KO} (p = 0.0058; U: 62, n_{WT} = 7, n_{KO} = 10) relative to GluA3^{WT}. See ***Figure 8—figure supplement 1***. (**B**) Quantification of median intensities per image for data in panel A. CtBP2 intensity increased in GluA3^{KO} (p = 0.0001; U: 17, n_{WT} = 14, n_{KO} = 13); GluA2 intensity decreased in GluA3^{KO} (p = 0.01; U: 143, n_{WT} = 14, n_{KO} = 13); and GluA4 intensity decreased in GluA3^{KO} (p = 5e^{-6}; U: 6, n_{WT} = 14, n_{KO} = 13). (**C**) Increase in CtBP2 (p = 5e^{-5}; U: 14, n_{WT} = 14, n_{KO} = 13) and GluA4 median density per synapse (p = 5e^{-6}; U: 6, n_{WT} = 14, n_{KO} = 13) in GluA3^{KO} relative to GluA3^{WT}, but not GluA2 (p = 0.63; U: 101, n_{WT} = 14, n_{KO} = 13). (**D**) Increase in GluA4:GluA2 intensity ratio in GluA3^{KO} relative to GluA3^{WT} (p = 6e^{-7}; U: 0, n_{WT} = 14, n_{KO} = 13). Mann-Whitney two-tailed U-test; ** p < 0.01, *** p < 0.001, ns: not significant.

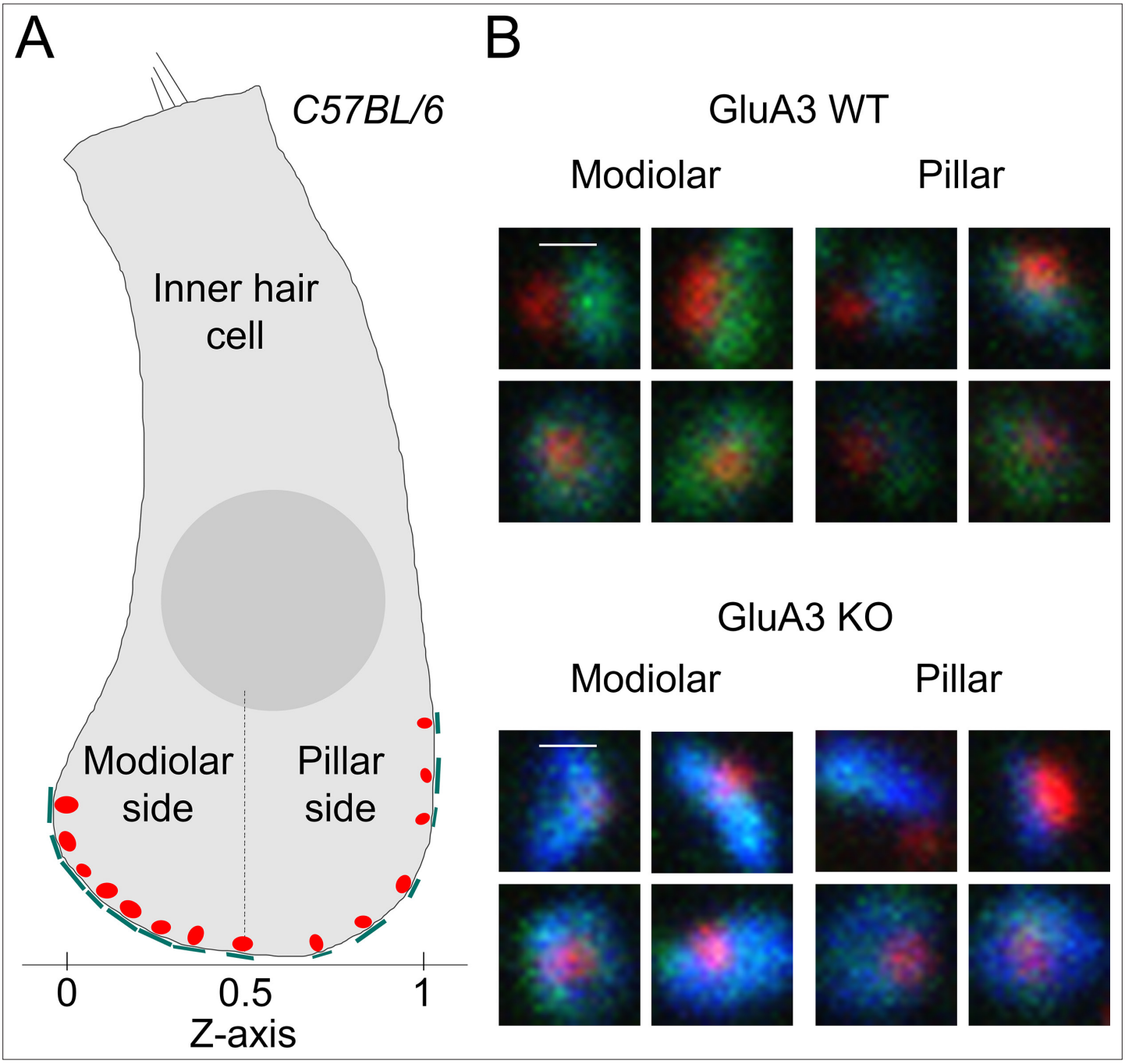

Figure 8—figure supplement 1. Modiolar-, pillar-side groupings and example synapses from GluA3^{WT} and GluA3^{KO}. (**A**) Schematic of an inner hair cell (IHC) when mounted with long axis parallel to the glass coverslip, such that the modiolar–pillar dimension of the cell is orthogonal to the coverslip. Per image, the synapses were divided into modiolar and pillar groups on either side of a dividing line defined by the midway point of the spatial extent of synapses in the modiolar–pillar dimension (*Z*-axis) of the image volume. (**B**) Examples of modiolar- and pillar-side synapses in GluA3^{WT} (upper) and GluA3^{KO} (lower). (**C**) Examples of modiolar- and pillar-side synapses in GluA3^{KO}.

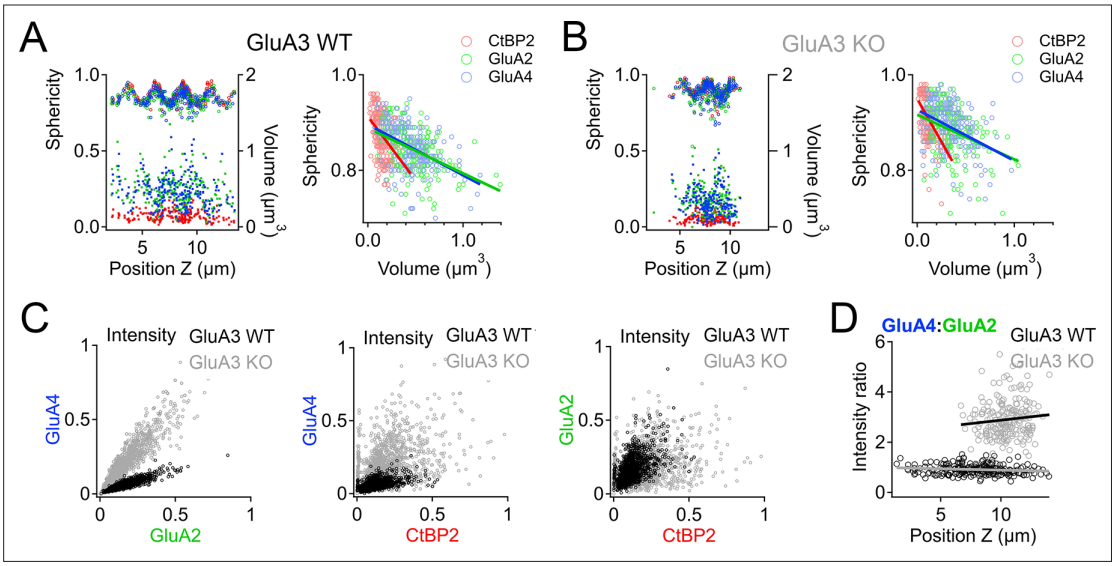

Figure 9. Spatial trends of synapse sphericity, volume, and α-amino-3-hydroxy-5-methyl-4-isoxazole propionic acid receptor (AMPAR) subunit relative abundance in the organ of Corti. (**A**) Volume and sphericity per synapse vs. *Z*-axis position for an exemplar GluA3^{WT} image from ***Figure 7*** showing spatial oscillations in CtBP2, GluA2, and GluA4. Right: Inverse relationship between synapse sphericity and volume for CtBP2, GluA2, and GluA4. (**B**) For GluA3^{KO}, as in panel A. (**C**) Left: Normalized intensity of GluA4 vs. normalized intensity of GluA2 for GluA3^{WT} (black) and GluA3^{KO} (gray). Center: Normalized intensity of GluA4 vs. normalized intensity of CtBP2. Right: Normalized intensity of GluA2 vs. normalized intensity of CtBP2. (**D**) GluA4:GluA2 intensity ratio vs. *Z*-axis position. Panels C and D for six WT and six KO images from the mid-cochlea.